International Forum on Aeroelasticity and Structural Dynamics
IFASD 2024
17-21 June 2024, The Hague, The Netherlands

FROM MULTIVARIATE RANDOM LOADS TO DETERMINISTIC LOAD DISTRIBUTIONS: AN EXACT METHOD FOR AEROELASTIC DESIGN

Carlo Aquilini[1], Gabriele Grasso[1], Cyrille Vidy[1]

[1] Airbus Defence and Space GmbH, Rechliner Straße, 85077 Manching, Germany

Keywords: buffet, random loads, turbulence, design, nodal loads, stress

Abstract: Multivariate random loads may arise from either a stationary Gaussian process, like stochastic or continuous gust, or from a random process, such as buffet. Buffet phenomena are important when the separated air flow induces strong fluctuating pressures on aircraft components. These loads need careful assessment during aircraft design, especially for fighters flying at high angles of attack and in the transonic regime, as well as for general aviation and transport aircraft.

This paper introduces an exact method for Aeroelastic design, specifically focusing on determining distributions of deterministic quasi-static nodal loads from integrated load cases obtained from the stochastic problem. Balanced and quasi-static load distributions are required by the stress office in order to size the affected structural components.

The methodology outlined in this paper builds on the work by Aquilini & Parisse [1], which provides a comprehensive method for predicting *n*-dimensional combined loads in the presence of massively separated flows. The methodology in [1] obtains a finite number of design load cases, by discretizing the *n*-dimensional design ellipsoid of equal probability with a semiregular polyhedron, a transformed small rhombicuboctahedron.

The present paper extends and concludes the work in [1] by determining distributions of deterministic nodal loads for each selected load case. The exactness of this method allows it to be applied to any load case that satisfies the equation of the multidimensional design load envelope. Thus, the load case selection is not confined to the vertices of the small rhombicuboctahedron but can utilize any discretisation of the ellipsoid. Moreover, this approach is versatile, applicable not only to buffeting but also to various stochastic problems, like continuous turbulence. To manage load case complexity, a reduction strategy is suggested, contributing to obtaining a reasonable and meaningful number of design load cases.

The paper concludes with examples showcasing the successful application of this method in real-world scenarios and its impact on the traditional Aeroelastic design.

1 INTRODUCTION

Fuselage strakes and wing leading-edge extensions are commonly used to improve the high-lift characteristics of fighters. They generate an unsteady flow field characterised by complex vortical patterns which affect loads and vibration of aircraft components downstream, leading to buffeting

(see [2]). For this reason, optimising fighter performances requires extensive analysis through simulations and testing also addressing buffeting aspects, which can otherwise cause premature structural failures ([3], [4]).

Given the stochastic nature of the phenomenon, the analysis of buffet results leads to physical quantities in the form of random variables. Particularly important is the derivation of the load covariance matrix, required for generating load envelopes, which are used to demonstrate compliance against aircraft allowable loads (see [1]). Multivariate random loads also arise from stationary Gaussian processes, such as the stochastic or continuous gust, or as a consequence of the separated air flow inducing fluctuating pressures on aircraft components. An example is the buffeting of the horizontal tail plane due to local flow separations at the wing for general aviation and commercial transport aircraft ([5], [6]).

Typically, the stress office requires distributions of balanced and quasi-static nodal loads in order to accurately size the aircraft structure. Unfortunately, the stochastic analysis leads to integrated loads and the corresponding deterministic nodal loads are not directly available. Equivalent deterministic load cases are historically employed to meet the requirements of the stress office, utilizing approximate procedures that entail iterative processes. This paper proposes an exact method for deriving deterministic quasi-static nodal loads directly from the stochastic analysis, eliminating the need for these approximations.

The structure of the paper is as follows. Chapter 2 outlines the methodology employed, while Chapter 3 showcases the successful application of this method in two distinct scenarios. Furthermore, a reduction strategy is suggested for managing load case complexity and contributing to obtaining a reasonable and meaningful number of design load cases.

2 THEORY

2.1 Buffeting in modal space

Let us consider the transfer function of the aeroelastic system described in modal space as (cf. [7])

$$\mathbf{H}(j\omega) = \left[-\omega^2\widetilde{\mathbf{M}} + j\omega\widetilde{\mathbf{B}} + (1+jg)\widetilde{\mathbf{K}} - q_\infty\widetilde{\mathbf{Q}}(Ma,k)\right]^{-1} \tag{1}$$

where ω is the circular frequency, $\widetilde{\mathbf{M}}$ the generalized mass, $\widetilde{\mathbf{B}}$ the modal damping, g the structural damping, $\widetilde{\mathbf{K}}$ the generalized stiffness, q_∞ the dynamic pressure, $\widetilde{\mathbf{Q}}(Ma,k)$ the generalized aerodynamic forces. The latter are function of the Mach number Ma and the reduced frequency $k = \omega\bar{c}/(2U_\infty)$, where $\bar{c}$ is the reference length and U_∞ is the free stream velocity.

In case the deterministic external forcing $\mathbf{F}_g$ is acting on the system of transfer function $\mathbf{H}(j\omega)$, the modal amplitudes can be derived as $\boldsymbol{\xi} = \mathbf{H}(j\omega)\boldsymbol{\Phi}^\intercal\mathbf{F}_g$, where $\boldsymbol{\Phi}$ is the (real) modal matrix.

If $\mathbf{F}_g$ is a random vector with spectrum $\mathbf{S}_{f_g}(j\omega)$, using the stochastic approach described in [1] and valid for wide-sense stationary stochastic processes (see [8], pp. 297-298), we obtain the spectrum of the modal amplitudes $\mathbf{S}_\xi(j\omega)$ as

$$\mathbf{S}_\xi(j\omega) = \mathbf{H}(j\omega)\boldsymbol{\Phi}^\intercal\mathbf{S}_{f_g}(j\omega)\boldsymbol{\Phi}\mathbf{H}(j\omega)^\dagger \tag{2}$$

where $\mathbf{H}(j\omega)^\dagger$ is the conjugate transpose of $\mathbf{H}(j\omega)$. Indeed, if $\mathbf{Y} = \mathbf{A}\mathbf{X}$ and $\mathbf{X}$ is a random vector whose spectrum is $\mathbf{S}_X(j\omega)$, its covariance is $\mathrm{Cov}(\mathbf{X})$ and $\mathbf{A}$ is a matrix, then $\mathbf{S}_Y(j\omega)$=$\mathbf{A}\mathbf{S}_X(j\omega)\mathbf{A}^\intercal$ and $\mathrm{Cov}(\mathbf{Y})$=$\mathbf{A}\mathrm{Cov}(\mathbf{X})\mathbf{A}^\intercal$ (cf. [8], p. 329).

The covariance matrix of the modal amplitudes is the integral of the spectrum in Eq. (2) (cf. [8], pp. 327-328)

$$\mathrm{Cov}(\boldsymbol{\xi}) = \frac{1}{2\pi}\int_{-\infty}^{+\infty} \mathbf{S}_{\xi}(j\omega)\mathrm{d}\omega \tag{3}$$

The covariance of the physical displacements can be obtained in analogy to $\mathbf{u} = \boldsymbol{\Phi}\boldsymbol{\xi}$ as

$$\mathrm{Cov}(\mathbf{u}) = \boldsymbol{\Phi}\mathrm{Cov}(\boldsymbol{\xi})\boldsymbol{\Phi}^{\intercal} \tag{4}$$

and nodal loads can be recovered by employing the modal displacement method ([9], pp. 641-650) as $\mathbf{Y} = \mathbf{K}\mathbf{u}$, where $\mathbf{K}$ is the stiffness matrix of the system, and their covariance is

$$\mathrm{Cov}(\mathbf{Y}) = \mathbf{K}\mathrm{Cov}(\mathbf{u})\mathbf{K}^{\intercal} = \mathbf{K}\boldsymbol{\Phi}\mathrm{Cov}(\boldsymbol{\xi})\boldsymbol{\Phi}^{\intercal}\mathbf{K}^{\intercal} \tag{5}$$

Finally, the integrated loads are obtained by summing up the nodal loads at specific monitoring stations, by using a transformation matrix $\mathbf{T}$ which rotates the nodal loads in the local coordinate system proper to each monitoring station and integrates them as $\mathbf{Y}_{MS} = \mathbf{T}\mathbf{Y}$. The covariance is

$$\mathrm{Cov}(\mathbf{Y}_{MS}) = \mathbf{T}\mathrm{Cov}(\mathbf{Y})\mathbf{T}^{\intercal} = \mathbf{T}\mathbf{K}\boldsymbol{\Phi}\mathrm{Cov}(\boldsymbol{\xi})\boldsymbol{\Phi}^{\intercal}\mathbf{K}^{\intercal}\mathbf{T}^{\intercal} = \mathbf{G}\mathrm{Cov}(\boldsymbol{\xi})\mathbf{G}^{\intercal} \tag{6}$$

where $\mathbf{G} = \mathbf{T}\mathbf{K}\boldsymbol{\Phi}$.

For Gaussian distributed combined loads, $\mathbf{Y}_{MS}$ lies on an *n*-dimensional quadric surface of equation

$$(\mathbf{Y}_{MS} - (\mathbf{Y}_{MS})_0)^{\intercal}\mathrm{Cov}(\mathbf{Y}_{MS})^{-1}(\mathbf{Y}_{MS} - (\mathbf{Y}_{MS})_0) = Q_n \tag{7}$$

which represents an ellipsoid, since the covariance matrix is positive definite and therefore also its inverse is positive definite (see [1]). It is the locus of points with the same probability density and it is *n*-dimensional since it represents combinations of at most three forces and three moments at multiple monitoring stations. The ellipsoid is translated of the steady-state loads $(\mathbf{Y}_{MS})_0$, which are added linearly to the incremental loads $\mathbf{Y}'_{MS}$. From now on, it is convenient to translate the coordinate system as $\mathbf{Y}'_{MS} = \mathbf{Y}_{MS} - (\mathbf{Y}_{MS})_0$, in order to have the centre of the ellipsoid in the origin and write the new coordinates without primes.

2.2 Deterministic nodal load distributions

By following given design guidelines, we can discretize the ellipsoid described by Eq. (7), select a specific number of design load cases $\mathbf{Y}_{MS}$ and derive the corresponding nodal load distributions for stress analysis.

If the matrix $\mathbf{G}$ is invertible, both the modal amplitudes $\boldsymbol{\xi}$ and the integrated loads $\mathbf{Y}_{MS}$ satisfy the same quadratic form Q_n

$$\boldsymbol{\xi}^{\intercal}\mathrm{Cov}(\boldsymbol{\xi})^{-1}\boldsymbol{\xi} = \mathbf{Y}_{MS}^{\intercal}\mathrm{Cov}(\mathbf{Y}_{MS})^{-1}\mathbf{Y}_{MS} = Q_n \tag{8}$$

Eq. (8) holds because the inverse of Eq. (6) is $\mathrm{Cov}(\mathbf{Y}_{MS})^{-1} = (\mathbf{G}^{\intercal})^{-1}\mathrm{Cov}(\boldsymbol{\xi})^{-1}\mathbf{G}^{-1}$ and given that $\mathbf{Y}_{MS} = \mathbf{G}\boldsymbol{\xi} \Rightarrow \mathbf{Y}_{MS}^{\intercal} = \boldsymbol{\xi}^{\intercal}\mathbf{G}^{\intercal}$, we obtain $\mathbf{Y}_{MS}^{\intercal}\mathrm{Cov}(\mathbf{Y}_{MS})^{-1}\mathbf{Y}_{MS} = \mathbf{Y}_{MS}^{\intercal}(\mathbf{G}^{\intercal})^{-1}\mathrm{Cov}(\boldsymbol{\xi})^{-1}\mathbf{G}^{-1}\mathbf{Y}_{MS} = (\mathbf{G}\boldsymbol{\xi})^{\intercal}(\mathbf{G}^{\intercal})^{-1}\mathrm{Cov}(\boldsymbol{\xi})^{-1}\mathbf{G}^{-1}(\mathbf{G}\boldsymbol{\xi}) = \boldsymbol{\xi}^{\intercal}\mathrm{Cov}(\boldsymbol{\xi})^{-1}\boldsymbol{\xi}$. Therefore, the modal amplitudes are $\boldsymbol{\xi} = \mathbf{G}^{-1}\mathbf{Y}_{MS}$. Furthermore, there exists an alternative representation for $\boldsymbol{\xi}$ given by

$$\boldsymbol{\xi} = \mathrm{Cov}(\boldsymbol{\xi})\mathbf{G}^{\intercal}\mathrm{Cov}(\mathbf{Y}_{MS})^{-1}\mathbf{Y}_{MS} = \mathrm{Cov}(\boldsymbol{\xi})\mathbf{G}^{\intercal}(\mathbf{G}\mathrm{Cov}(\boldsymbol{\xi})\mathbf{G}^{\intercal})^{-1}\mathbf{Y}_{MS} \tag{9}$$

Eq. (9) is obtained by substituting $\mathbf{Y}_{MS}^{\intercal} = \boldsymbol{\xi}^{\intercal}\mathbf{G}^{\intercal}$ into Eq. (8) and performing some manipulations.

In general, $\mathbf{G} \in \mathcal{R}^{n\times h}$ and $\mathbf{Y}_{MS} \in \mathcal{R}^{n}$. Let $\mathbf{G}^{+}$ denote the Moore-Penrose pseudoinverse of $\mathbf{G}$ and $\mathbf{I}$ the identity matrix. If $\mathbf{G}\mathbf{G}^{+}\mathbf{Y}_{MS} = \mathbf{Y}_{MS}$, then any vector in the form of $\boldsymbol{\xi} = \mathbf{G}^{+}\mathbf{Y}_{MS} + (\mathbf{I} - \mathbf{G}^{+}\mathbf{G})\mathbf{y}$ is a solution of $\mathbf{Y}_{MS} = \mathbf{G}\boldsymbol{\xi}$, where $\mathbf{y} \in \mathcal{R}^{h}$ is an arbitrary vector (cf. [10]). If the $\mathrm{rank}(\mathbf{G}) = h$, the solution $\boldsymbol{\xi} = \mathbf{G}^{+}\mathbf{Y}_{MS}$ is unique, because $(\mathbf{I} - \mathbf{G}^{+}\mathbf{G}) = \mathbf{0}$. Similar to the case where $\mathbf{G}$ is invertible, this solution satisfies Eq. (8) and Eq. (9) is still verified. If the $\mathrm{rank}(\mathbf{G}) = n < h$, then $\mathbf{Y}_{MS} = \mathbf{G}\boldsymbol{\xi}$ is indeterminate with ∞^{h-n} solutions, depending on the choice of $\mathbf{y}$. In this latter case, the special solution $\boldsymbol{\xi} = \mathbf{G}^{+}\mathbf{Y}_{MS}$ obtained for $\mathbf{y} = \mathbf{0}$ is the one with minimum Euclidean norm but may not satisfy the quadratic form Q_n. However, there always exists an arbitrary vector $\mathbf{y}$ that yields a specific solution $\boldsymbol{\xi}$ which satisfies the ellipsoid equation and this solution is still given by Eq. (9)[1].

This solution ensures that the statistical correlation between modes is preserved, maintaining their physical meaning. Importantly, the solution obtained through this method is both unique and exact.

The distributions of balanced quasi-static nodal loads relative to the selected load cases $\mathbf{Y}_{MS}$ are finally obtained as

$$\mathbf{Y} = \mathbf{K}\boldsymbol{\Phi}\boldsymbol{\xi} = \mathbf{K}\boldsymbol{\Phi}\mathrm{Cov}(\boldsymbol{\xi})\mathbf{G}^{\mathsf{T}}(\mathbf{G}\mathrm{Cov}(\boldsymbol{\xi})\mathbf{G}^{\mathsf{T}})^{-1}\mathbf{Y}_{MS} \tag{10}$$

Eq. (10) generally applies to any load case $\mathbf{Y}_{MS} = (\mathbf{Y}_{MS})_0 + \mathbf{Y}'_{MS}$ comprehensive of the mean or steady-state components $(\mathbf{Y}_{MS})_0$ and of the incremental loads $\mathbf{Y}'_{MS}$. This implies that it is possible to recover distributions of balanced quasi-static nodal loads from any point on the translated *n*-dimensional design load envelope. Because of the linearity of the formulation, the steady-state components $(\mathbf{Y}_{MS})_0$ can be also treated as an additional load case. Once the steady nodal loads are obtained through Eq. (10), they can be added to all dynamic nodal load distributions separately.

In conclusion, Eqs. (9) and (10) can be generally applied to recover the modal amplitudes $\boldsymbol{\xi}$ and the nodal loads $\mathbf{Y}$ from the load cases $\mathbf{Y}_{MS}$. The only requirement is that $\mathrm{Cov}(\boldsymbol{\xi})$ is positive definite.

3 APPLICATIONS

The proposed methodology is applicable to various stochastic problems, including continuous turbulence, where the right-hand side of the equation is a stationary Gaussian random input, that is the Von Kármán spectrum of the turbulence (see [11]). Also in this case, the analysis yields a certain number of load cases $\mathbf{Y}_{MS}$, which satisfy Eq. (8) and can be directly used in Eq. (10) for obtaining balanced nodal load distributions.

It is evident that the down-selection of the load cases from Eq. (8) is a fundamental step for a good design. The methodology in [1] derives important points on the ellipsoid, like the points of tangency with the circumscribing *n*-orthotope, which are the maximum loads. It also obtains a finite number of design load cases, by discretizing the *n*-dimensional design ellipsoid of equal probability with a semiregular polyhedron, a transformed small rhombicuboctahedron. Eq. (10) can be employed both for the maxima of the ellipsoid and for the vertices of the small rhombicuboctahedron, in order to recover the relative distributions of nodal loads.

Different strategies can be used in order to select the most suitable load cases for the specific application and reduce the load cases to a minimum number relevant for design. For instance:

[1] Notably, the matrix $\mathbf{G}^{+}\mathbf{G}$ is a projector, because its eigenvalues are either 0 or 1. Consequently, $(\mathbf{I} - \mathbf{G}^{+}\mathbf{G})$ also acts as a projector and the equation $(\mathbf{I} - \mathbf{G}^{+}\mathbf{G})\mathbf{y} = \boldsymbol{\xi} - \mathbf{G}^{+}\mathbf{Y}_{MS}$ projects all vectors $\mathbf{y} \in \mathcal{R}^{h}$ in the space that contains $\boldsymbol{\xi}$ and $\mathbf{G}^{+}\mathbf{Y}_{MS}$. Therefore, by selecting $\mathbf{y} = \boldsymbol{\xi}$ and considering Eq. (9), we obtain $(\mathbf{I} - \mathbf{G}^{+}\mathbf{G})\boldsymbol{\xi} = \boldsymbol{\xi} - \mathbf{G}^{+}(\mathbf{G}\mathrm{Cov}(\boldsymbol{\xi})\mathbf{G}^{\mathsf{T}})(\mathbf{G}\mathrm{Cov}(\boldsymbol{\xi})\mathbf{G}^{\mathsf{T}})^{-1}\mathbf{Y}_{MS} = \boldsymbol{\xi} - \mathbf{G}^{+}\mathbf{Y}_{MS}$, thus verifying the original problem.

1. The maximum loads of the ellipsoid or its vertices are typically sufficient for the preliminary design, obtaining $2n$ design load cases (or $4n$ if we consider both the maxima and the vertices of the ellipsoid).
   Generally, it is useful to express Eq. (7) in function of its maxima and minima $\pm U_\sigma \boldsymbol{\sigma}_{Y_{MS}}$, where U_σ is a scalar factor (whose value depends on the specific application in order to have adequate coverage of all possible values of the Gaussian process) and $\boldsymbol{\sigma}_{Y_{MS}}$ is the diagonal matrix of the standard deviations of $\mathbf{Y}_{MS}$. Considering the correlation function $\mathrm{Cor}(\mathbf{Y}_{MS}) = \boldsymbol{\sigma}_{Y_{MS}}^{-1}\mathrm{Cov}(\mathbf{Y}_{MS})\boldsymbol{\sigma}_{Y_{MS}}^{-1}$ and $\boldsymbol{\sigma} = U_\sigma \boldsymbol{\sigma}_{Y_{MS}}\sqrt{\det\big(\mathrm{Cor}(\mathbf{Y}_{MS})\big)}$, the equation of the ellipsoid inscribed in the cuboid defined by the planes $\mathbf{Y}_{MS} = \pm U_\sigma \boldsymbol{\sigma}_{Y_{MS}}$ and centre in the origin is $\mathbf{Y}_{MS}^{\mathrm{T}}\mathbf{C}\mathbf{Y}_{MS} = 1$, with $\mathbf{C} = \det\big(\mathrm{Cor}(\mathbf{Y}_{MS})\big)(\boldsymbol{\sigma}^{-1}\mathrm{Cor}(\mathbf{Y}_{MS})^{-1}\boldsymbol{\sigma}^{-1})$. If the eigenvalues and eigenvectors of $\mathbf{C}$ are $\boldsymbol{\lambda}_n$ and $\boldsymbol{\Psi}$ respectively, then the coordinates of the vertices of the ellipse are $\mathbf{Y}_{MS_i} = \boldsymbol{\Psi}_i/\sqrt{\lambda_i}$ and the coordinates of its maxima are $\mathbf{Y}_{MS_i} = U_\sigma \boldsymbol{\sigma}_{Y_{MS}}\boldsymbol{\rho}_i$, where $\boldsymbol{\rho}_i$ is the i-th column of the correlation matrix $\mathrm{Cor}(\mathbf{Y}_{MS})$**.** By the half turn $\mathbf{Y}'_{MS} = -\mathbf{Y}_{MS}$ we obtain the symmetric coordinates with respect to the origin.
2. If more conservativism is required, it is possible to use the vertices of the transformed small rhombicuboctahedron, obtaining $n \cdot 2^n$ design load cases (see [1]). The coordinates of its vertices are $\mathbf{Y}_{MS} = \boldsymbol{\Psi}\sqrt{\boldsymbol{\lambda}_n}\mathbf{w}$, where $\boldsymbol{\lambda}_n$ and $\boldsymbol{\Psi}$ are the eigenvalues and eigenvectors of $\mathbf{C}$ and $\mathbf{w}$ are all distinct permutations of $\mathbf{w} \coloneqq \big(1+\sqrt{2}\big)^{-1}\big[\pm 1, \pm 1, \dots, \pm\big(1+\sqrt{2}\big)\big]$ (see [1]). It is then possible to reduce the overall number of design load cases by evaluating their correlation and, among the ones which have high correlation (i.e. above a selected threshold), retain only the load case with the highest norm. Indeed, highly correlated load cases generate very similar load distributions.
3. The reduction of the number of load cases is necessary especially when complex unsteady patterns need to be captured through a large number of monitoring stations. In this case a principal component analysis can be employed, extracting main loading components at aircraft or component level (see [12]).

The following paragraphs showcase the calculation of nodal loads for two different applications. The first is the buffeting of main landing gear doors of a commercial transport aircraft during the deployment and the retraction of the landing gears at approach and after take-off. The second application is related to the buffeting of the wing and the horizontal tail plane of an aeroelastic wind tunnel model of a generic fighter aircraft designed with the scope of validating numerical models and simulation results.

3.1 Main landing gear doors of a commercial transport aircraft

The turbulent flow created by the nose landing gear of a commercial transport aircraft during the approach and after take-off propagates further downstream and may induce unsteady aerodynamic loads on the main landing gear doors (Figure 1).

In the frame of the European Project AFLoNext, a dynamic model of an isolated main landing gear door of an Airbus A320 has been updated and validated with the results of a Ground Vibration Test and by using the Operational Modal Analysis based on existing flight test measurements (see [14]). CFD analyses using DES-type and other hybrid RANS-LES methods have been also performed for selected flight conditions and for different positions of the main and nose landing gears (see [15] and [16]).

The unsteady pressures sampled on the main landing gear doors surfaces have been finally employed in the aeroelastic analysis based on the one-way CFD-CSM coupling described in [1]. This led to the full characterisation of the dynamic behaviour of the doors under buffet loading and enabled the design, the manufacturing and flight testing of passive means for the reduction of vibration and loads of the doors during landing gear operations (see [14] and [17]).

The door under investigation is shown in Figure 2. It is connected to the keel beam with two hinges and one actuator (red triangles in Figure 2). Objective of this chapter is to derive distributions of deterministic nodal loads $\mathbf{Y}$ which lead to the maximum reaction forces $\mathbf{Y}_{MS} = (\mathbf{Y}_{MS})_0 + \mathbf{Y}'_{MS}$, sum of the steady state and dynamic components.

Figure 1: Airbus A320-212 with main landing gear doors open. Nose and main landing gears are in transit [13].

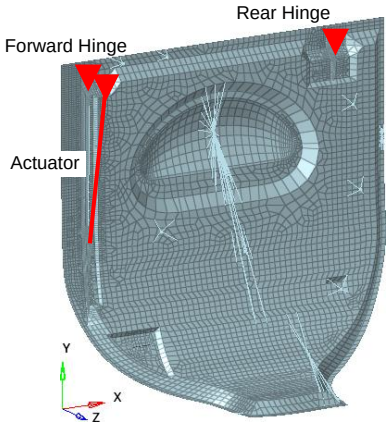

Figure 2: Main landing gear door FEM. Red triangles are the forward and rear hinges and the actuator fitting. The red line is the actuator.

Three monitoring stations are introduced in order to take into account the reaction forces F_x, F_y and F_z for the forward hinge, F_y and F_z for the rear hinge and the force F along the actuator.

The covariance matrix of the reaction forces $\mathrm{Cov}(\mathbf{Y}_{MS})$ can be derived from the covariance matrix of the modal amplitudes $\mathrm{Cov}(\boldsymbol{\xi})$ according to Eq. (6) and the ellipsoid of equal probability density is six-dimensional according to Eq. (8). The projections of the ellipsoid are shown in black in Figure 3. The red lines represent the planar projections of the circumscribing small rhombicuboctahedron, while the blue dots represent the maximum reaction forces. The ellipses are translated of the static loading components.

If we select the maximum reaction forces from Eq. (8) (represented by the blue dots of Figure 3), $\mathbf{Y}_{MS}$ includes 12 dynamic and one steady-state design load cases. Quasi-static nodal loads relative to the 13 selected load cases are derived from Eq. (10). The three force components of the load distributions are shown for each specific design load case from Figure 4 to Figure 6. They are normalised by the maximum force component in each specific load case, and load cases that are symmetric about the origin are omitted.

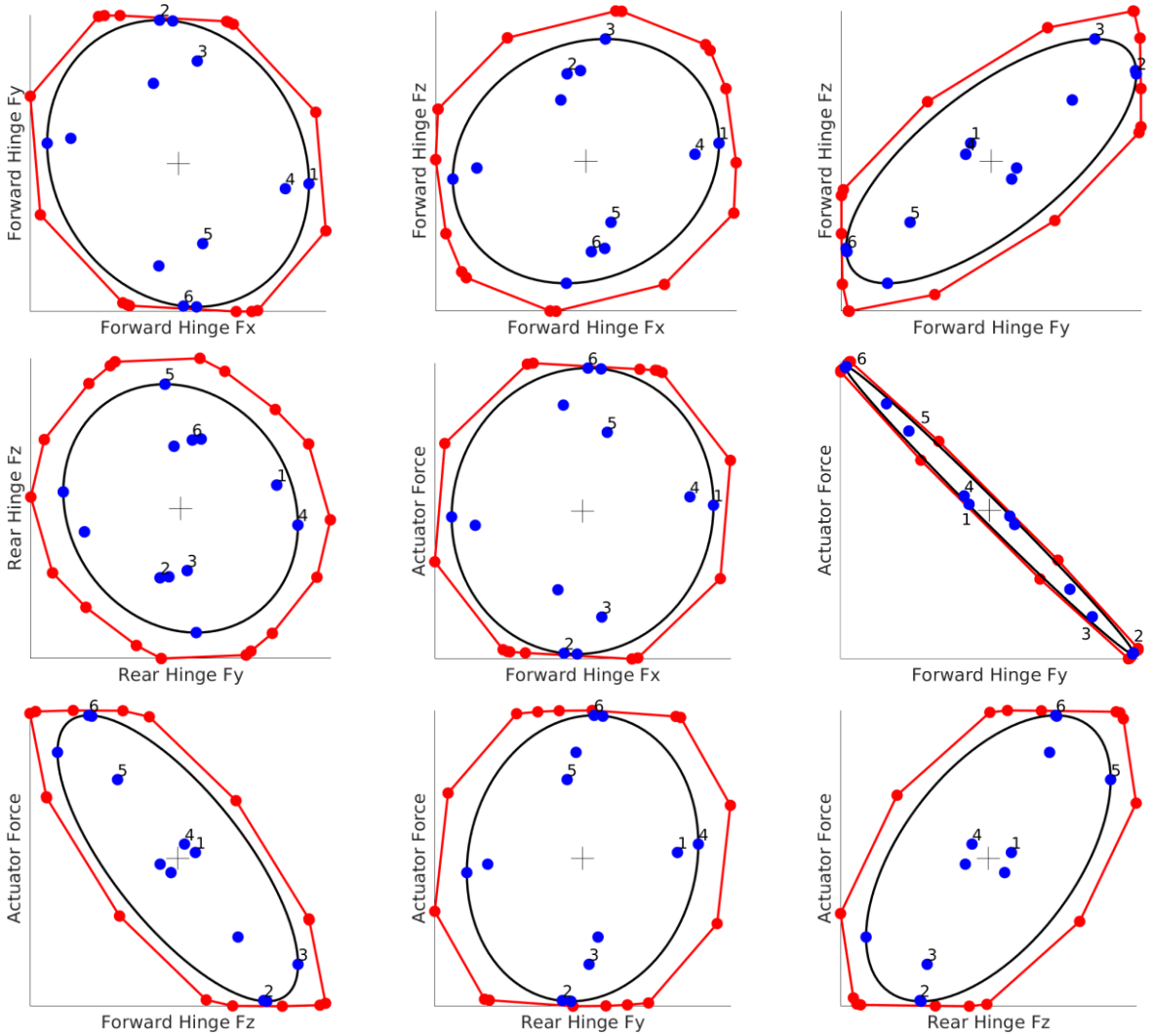

Figure 3: Projections of the 6-dimensional ellipsoid (black) with the circumscribing small rhombicuboctahedron (red) and maximum reaction forces (blue).

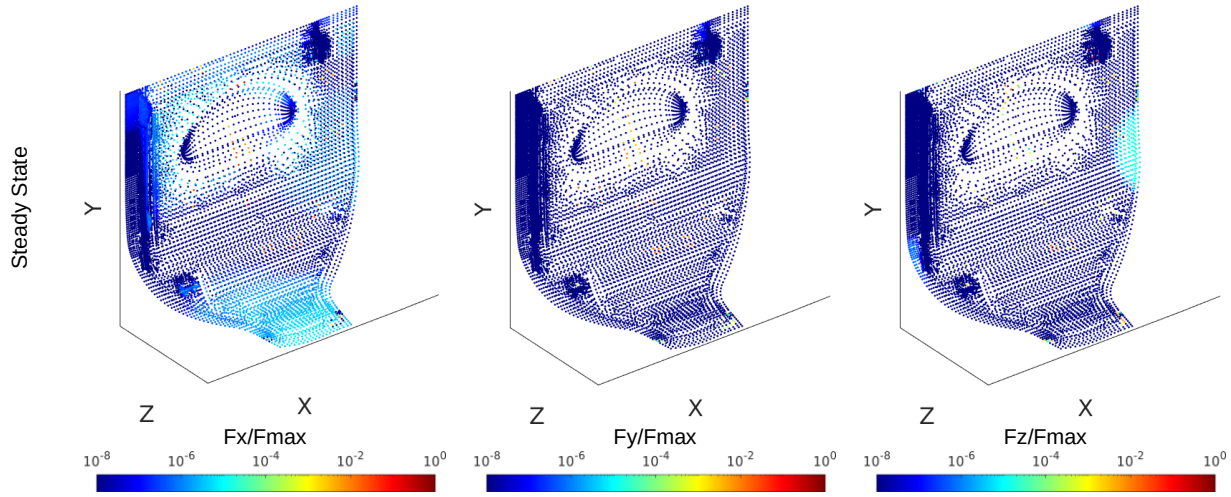

Figure 4: Nodal load distributions for the steady state load case.

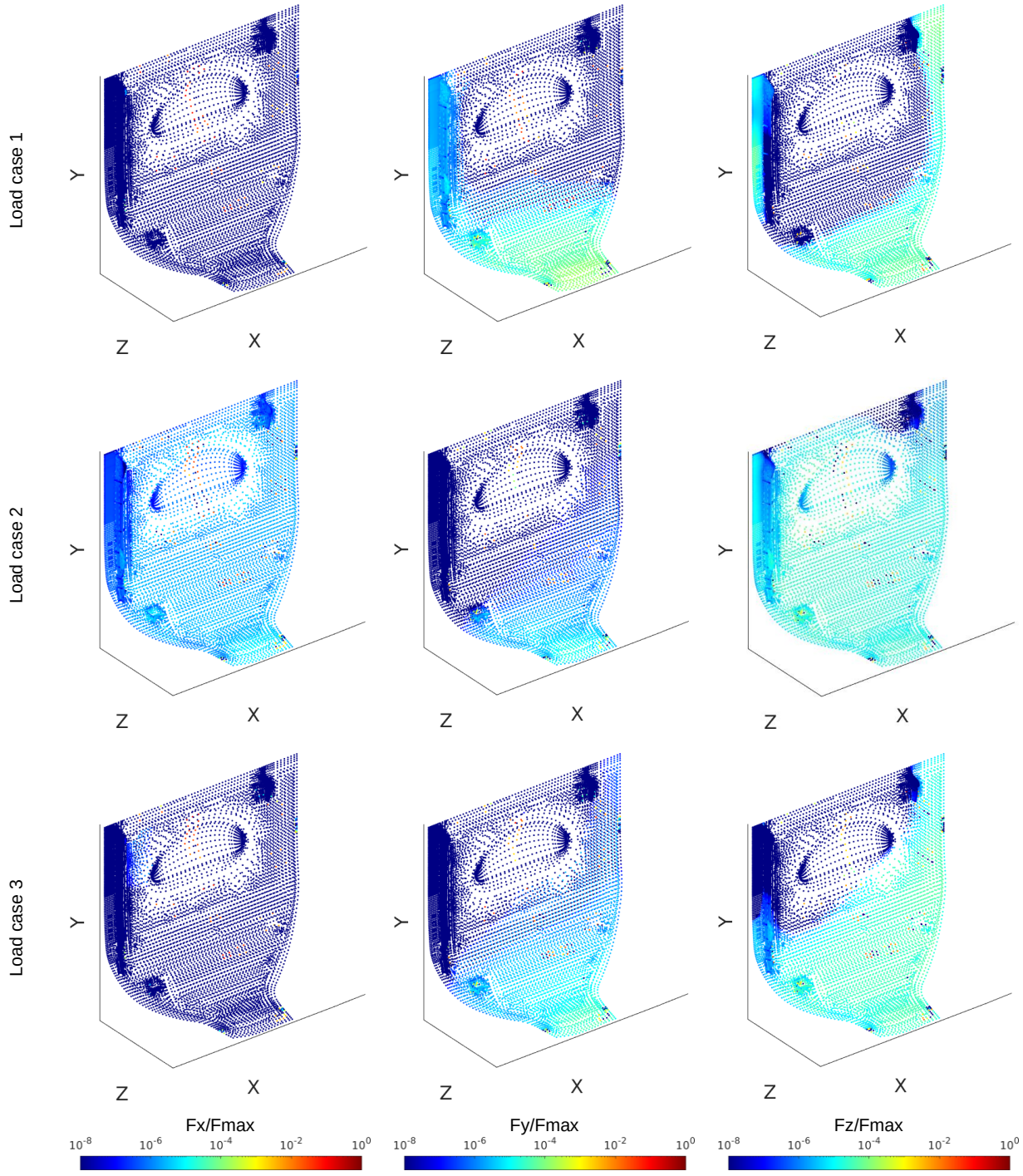

Figure 5: Nodal load distributions for the load cases 1, 2 and 3.

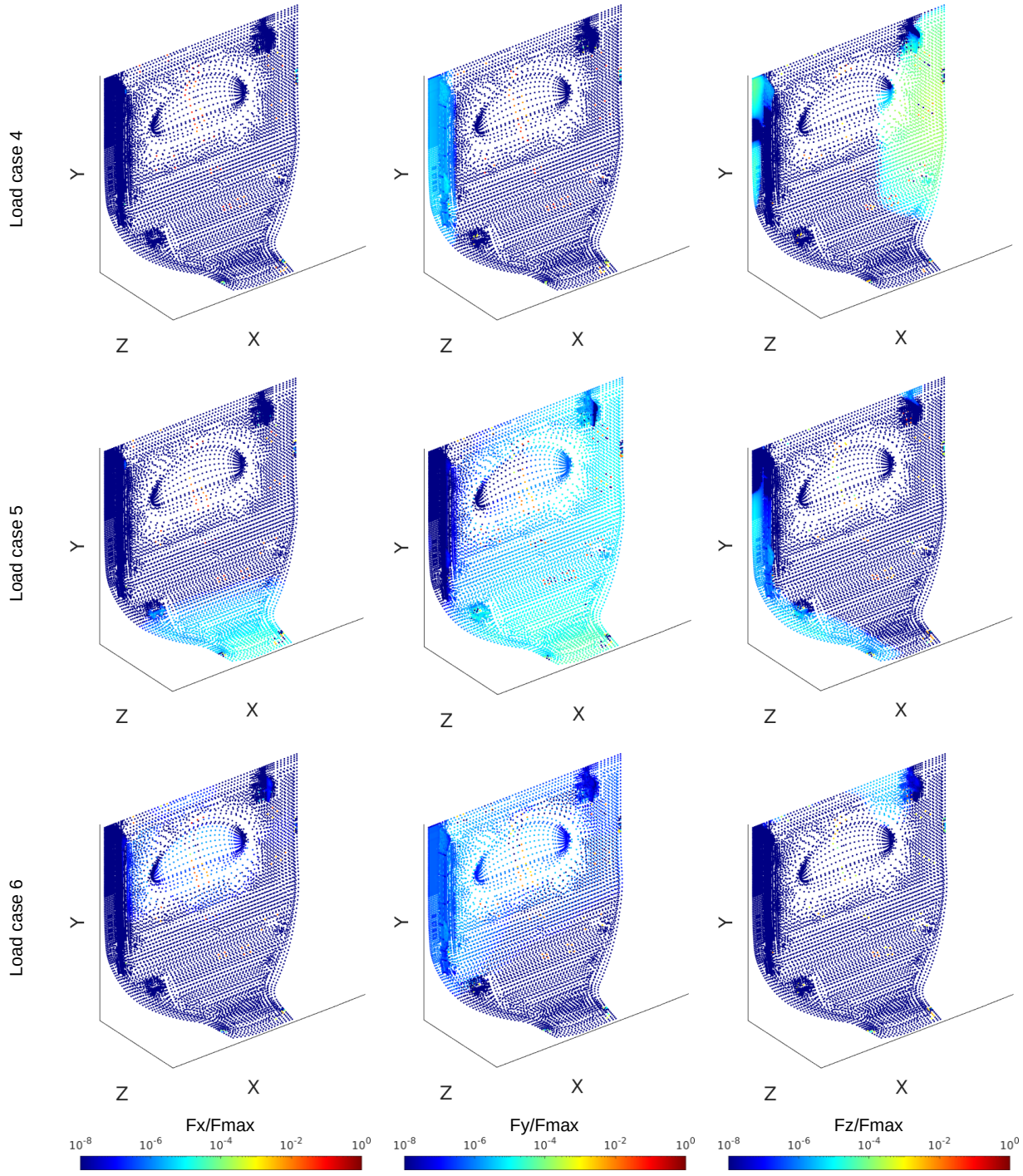

Figure 6: Nodal load distributions for the load cases 4, 5 and 6.

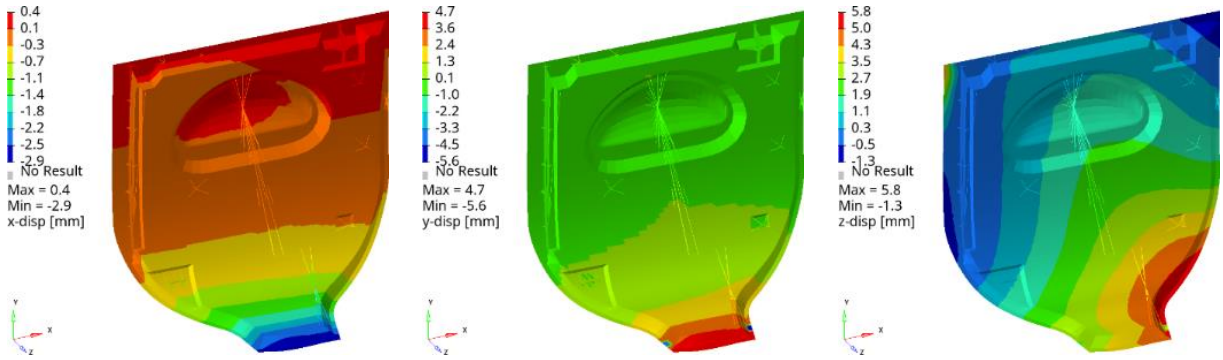

Figure 7: Difference of the structural deformations in the three axes obtained using the mean of the aerodynamic forces and the nodal loads of the steady state load case from Eq. (10).

Given the exactness of the methodology, the nodal loads are perfectly balanced with the reaction forces (i.e. the sum of the forces and the sum of the moments relative to a common point are zero). Moreover, the integrals of the nodal forces over the three defined monitoring stations (i.e. $\mathbf{Y}_{MS} = \mathbf{TY}$) are equal to the initial reaction forces. Qualitatively, nodes with greater mass and those that are constrained experience larger nodal forces. This aligns with our expectations.

The nodal forces and moments obtained can be directly applied in stress analyses to size the fittings for the primary structure. Figure 7 depicts the difference between the structural deformations obtained in the three axes using two methods. The first method applies the mean of the aerodynamic forces directly to the FEM. The second method utilizes nodal loads obtained by applying Eq. (10) to the steady reaction forces at the hinges and actuator fitting. The observed relative difference is local and results from the modal approach inherent to this methodology, generally remaining below 5%.

3.2 Aeroelastic wind tunnel model of a generic fighter aircraft

The results of buffeting simulations and the methods developed for the fluid-structure coupling require validation with measurements in a wind tunnel. For this purpose, an aeroelastic wind tunnel model has been developed for experimental tail buffeting analysis by Katzenmeier et al. [18]. It is designed as a half-model configuration and consists of a rigid fuselage in aluminium with flexible wing and horizontal tail plane manufactured from 3D-printed polylactide (PLA) with 100% fill density (see Figure 8). The FEM of the wind tunnel model is shown in Figure 9.

Figure 8: Aeroelastic wind tunnel model on the turn table of the Wind Tunnel at the Technical University of Munich.

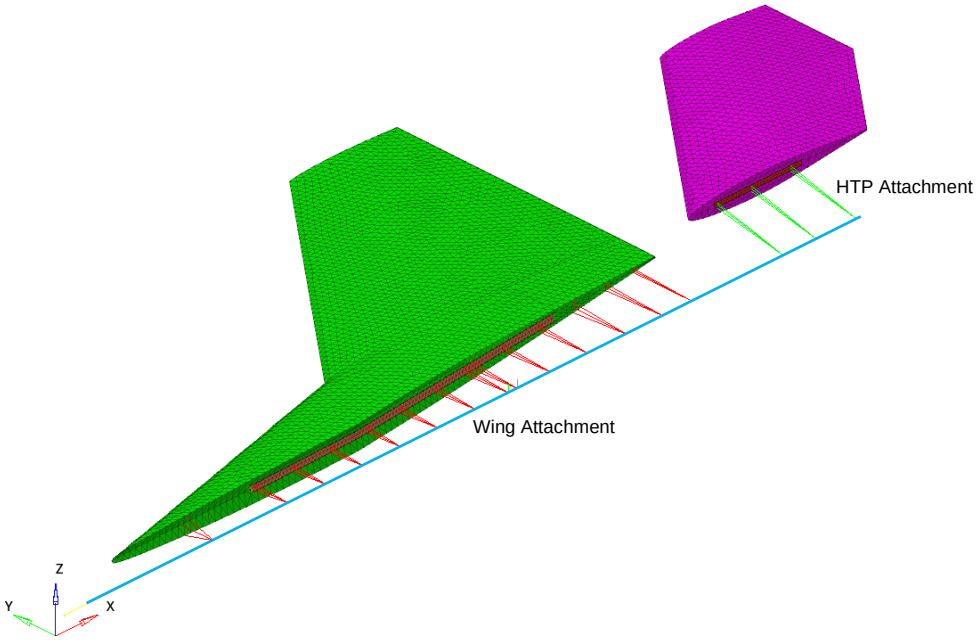

Figure 9: FEM of the aeroelastic wind tunnel model.

The model generates a highly unsteady flow field, characterised by two interacting vortices which burst over the wing and lead to vibration and loads on the wing and on the horizontal tail plane. The flow field has been computed using an Improved Delayed Detached Eddy Simulation turbulence approach with Spalart-Allmaras statistical modelling in the RANS zones (see [19]). The one-way coupling analysis follows the approach as described in [1] using a Proper Orthogonal Decomposition in order to reduce the size of the buffet excitation and therefore the computational efforts ([18], [20]). The analysis produces the covariance matrix of the modal amplitudes $\mathrm{Cov}(\boldsymbol{\xi})$, which can be used to compute the covariance matrix of the integrated loads $\mathrm{Cov}(\mathbf{Y}_{MS})$ through Eq. (6) and to draw the ellipsoid through Eq. (8). Given the selected design load cases, we recover the relative balanced quasi-static distributions of nodal loads from Eq. (10).

Three monitoring stations have been selected for sizing the wind tunnel model: the attachment of the HTP (red circles in Figure 10), the outboard wing and the outboard HTP (marked in red in Figure 10), defined at 50% of the respective chords. For all monitoring stations the shear F_z, the bending M_x and the torsion M_y are used for the selection of the load cases and therefore Eq. (8) is a nine-dimensional ellipsoid (Figure 11). The successful application of the methodology is shown by selecting the $9 \cdot 2^9 = 4608$ vertices of the small rhombicuboctahedron as design load cases.

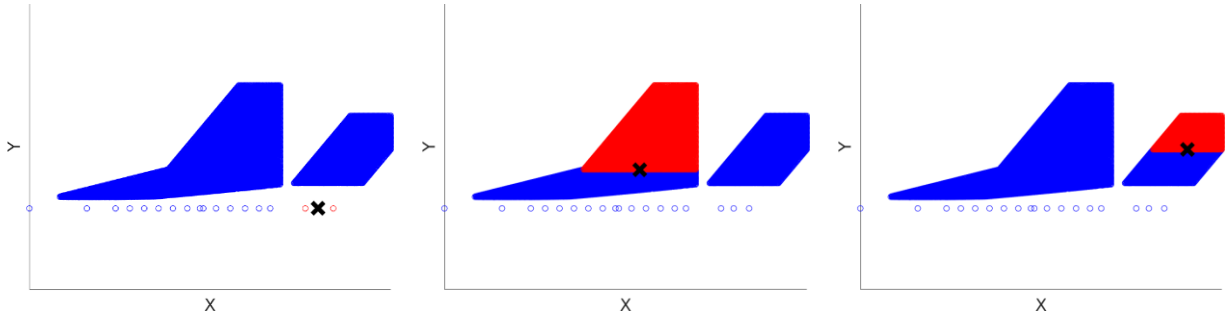

Figure 10: Three monitoring stations are selected. The horizontal tail plane attachment (red circles), the outer wing and the outer horizontal tail plane sections (marked in red). Shear, bending and torsion are considered.

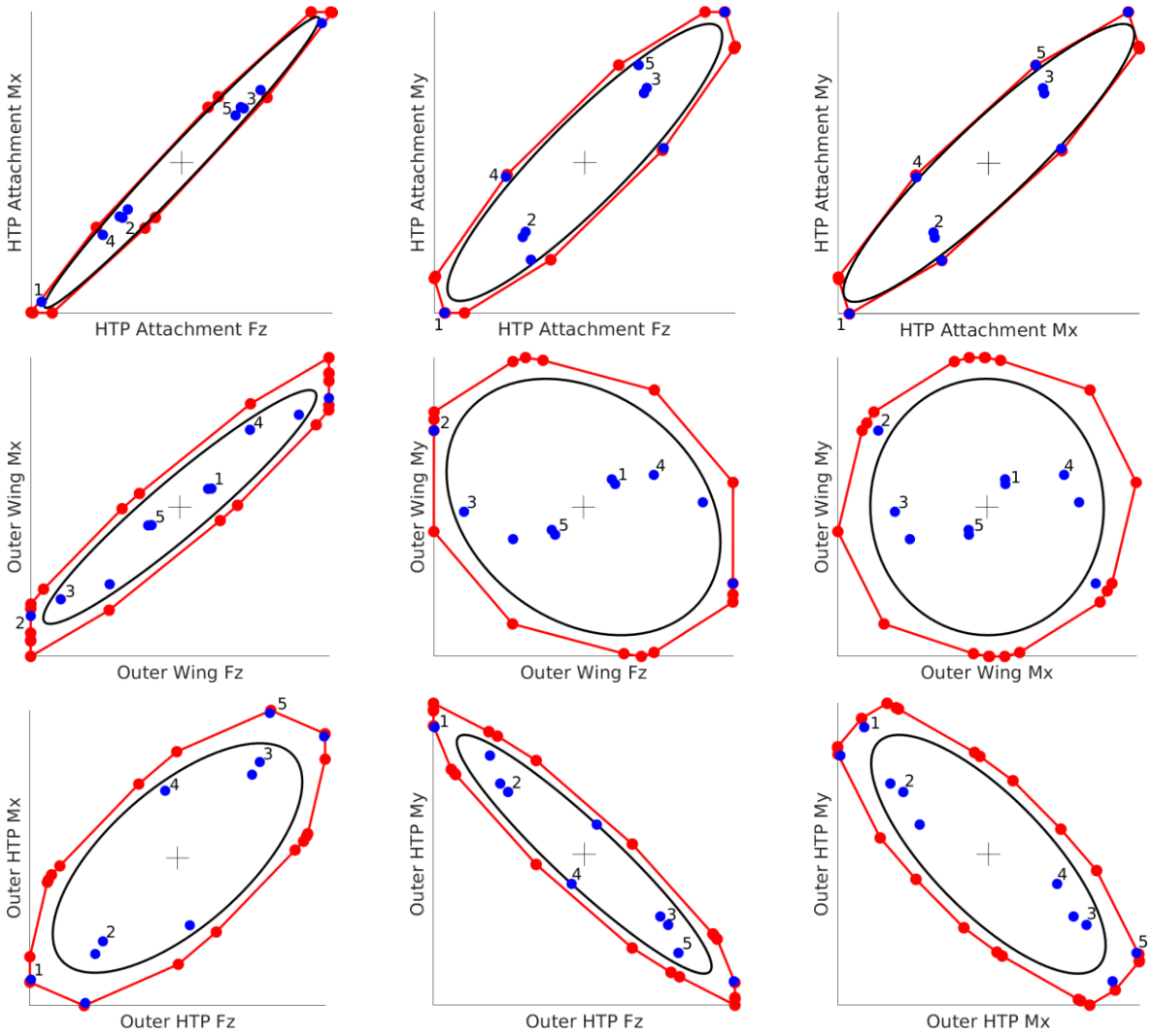

Figure 11: Projections of the 9-dimensional ellipsoid (black) with the circumscribing small rhombicuboctahedron (red) and the selected load cases (blue).

We analysed the ten load cases with the highest norm among those exceeding a correlation coefficient of 0.9 (represented by the blue dots in Figure 11). Load cases inducing significant outer wing torsion were excluded due to their high correlation with other high-norm cases. Figure 12 presents the relative nodal load distributions obtained using Eq. (10). These distributions are normalised by the maximum load within each specific load case, and load cases that are symmetric about the origin are omitted.

Consistently with the application described in Chapter 3.1, the nodal load distributions exhibit perfect balance. This means the sum of forces and the sum of moments relative to a chosen reference point both equal zero. Additionally, the integrals of the nodal forces over the three designated monitoring stations (i.e. $\mathbf{Y}_{MS} = \mathbf{TY}$) match the initial integrated loads.

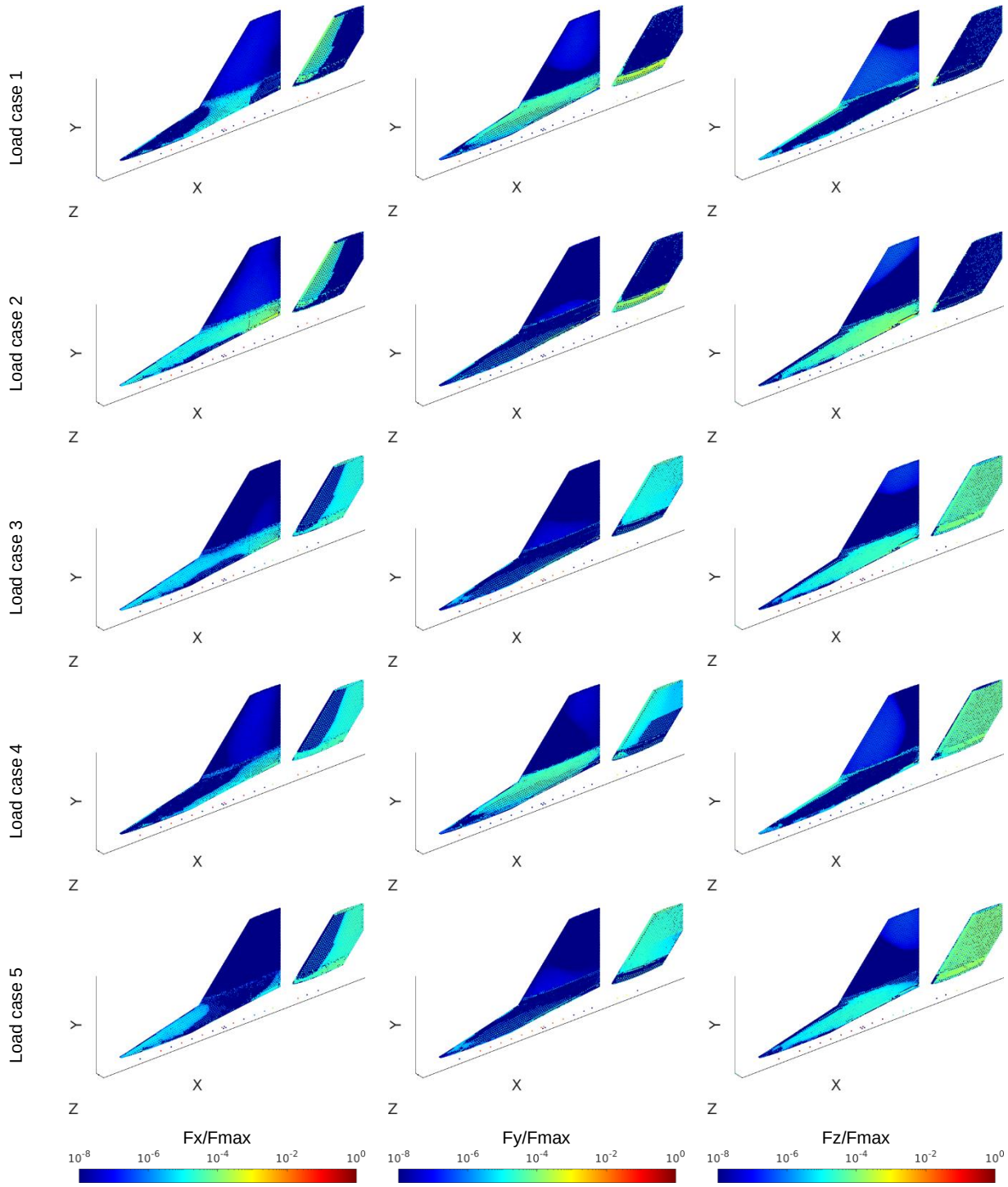

Figure 12: Nodal load distributions for the selected load cases.

4 CONCLUSIONS

This paper introduces an exact method for recovering distributions of deterministic quasi-static nodal loads specifically for stochastic aeroelastic applications. These loads are crucial to accurately size structural components affected by buffet and other unsteady aerodynamic phenomena.

The methodology builds upon the results presented in [1], where a comprehensive approach for predicting *n*-dimensional combined loads in the presence of massively separated flow is derived. This work extends the previous method by enabling the determination of deterministic nodal load distributions from each design load case.

The key aspects of this method are its exactness and versatility. The method is applicable to any load case which satisfies the equation of the multidimensional design load envelope. This always ensures accurate results against the traditional approaches which rely on approximate procedures in order to generate equivalent deterministic load cases. Moreover, the approach is not limited to buffeting phenomena but can be applied to various stochastic problems, including continuous turbulence.

A load case reduction strategy is suggested to manage load case complexity by selecting reasonable and meaningful design load cases, depending on the specific problem.

The paper concludes by showcasing successful applications of this method in two real-world scenarios. First the method is used to derive distributions of deterministic nodal loads for sizing the fittings of landing gear doors of a commercial transport aircraft subjected to buffeting during landing gear operations. In the second application, the method is employed to obtain nodal loads for sizing an aeroelastic wind tunnel model used for experimental tail buffeting analysis. These applications demonstrate the effectiveness of the proposed method in determining accurate nodal loads which can be directly used for stress analysis and proper structural design in aeroelastic problems.

ACKNOWLEDGEMENTS

Special thanks to Daniele Parisse for his insightful contribution in finding the arbitrary vector **y** in Chapter 2.2. He provided a key piece of the puzzle for our research.

We are also grateful to Lukas Katzenmeier for providing us with a photograph of the wind tunnel model and the modal amplitudes covariance matrix from his analysis.

REFERENCES

[1] Aquilini, C., Parisse, D. (2017). *A Method for Predicting Multivariate Random Loads and a Discrete Approximation of the Multidimensional Design Load Envelope.* IFASD 2017, Como, Italy.

[2] Ray, E. J., McKinney, L. W., Carmichael, J. G. (1973). *Maneuver and Buffet Characteristics of Fighter Aircraft*. NASA TN D-7131.

[3] Zimmerman, N. H., Ferman, M. A., Yurkovich, R. N., Gerstenkorn, G. (1989). *Prediction of Tail Buffet Loads for Design Application*. AIAA paper No. 89-1378.

[4] Anderson, W. D., Patel, S. R., Black, C. L. (2006). Low-Speed Wind Tunnel Buffet Testing on the F-22. *Journal of Aircraft* Vol. 43. No. 4. July-August 2006.

[5] Farokhi, S., Mauk, C. S., Locke, J. E. (1996). *Stochastic Modeling of Antisymmetric Buffet Loads on Horizontal Stabilizers in Massively Separated Flows*. DOT/FAA/AR-95/7. US Department of Transportation Federal Aviation Administration.

[6] Koopmans, W., Klabes, A., Gojny, M. H. (2022). *Wing-Tailplane Flow Interaction: Flight Test Data Analysis from Stall Flights*. IFASD 2022, Madrid, Spain.

[7] Rodden, W. P., Johnson, E. H. (1994). *MSC.Nastran Aeroelastic Analysis User's Guide Version 68*, p.71.

[8] Papoulis, A. (1991). *Probability, Random Variables, and Stochastic Processes*. McGraw-Hill, Inc. 3rd ed.

[9] Bisplinghoff, R. L., Ashley, H., Halfman, R. L. (1996). *Aeroelasticity*. New York: Dover Publications, Inc.

[10] Davis, P. J. (1979). *Circulant Matrices*. Ann Arbor, Michigan: John Wiley & Sons, Reprinted on Demand by University Microfilms International, pp. 44-59.

[11] European Union Aviation Safety Agency (2023). *Certification Specifications for Large Aeroplanes, CS-25, Amendment 28*, pp. 215-219.

[12] Vidy, C., Aquilini, C. (2024). *Robust Design Through Identification of Main Components from Multivariate Random Loads*. IFASD 2024, The Hague, The Netherlands.

[13] *CAA Airbus A320 Potters-2.jpg - Wikimedia Commons*. (2011). https://commons.m.wikimedia.org/wiki/File:CAA_Airbus_A320_Potters-2.jpg.

[14] Abarca, R., Aquilini, C., Lubrina, P., Peng, S. H., Schwochow, J. (2019). *Aeroelastic Coupling and Control Means for Reduction of Main Landing Gear Doors Responses under Operational Conditions*. IFASD 2019, Savannah, Georgia, USA.

[15] Peng, S. H., Jirasek, A., Dalenbring, M., Eliasson, M. (2016). *Aerodynamic excitation on MLG door exposed to vortices emanating from NLG of an aircraft model*. AIAA Paper 2016-4043. AIAA Aviation 2016. Washington DC.

[16] Tomac, M., Rizzi, A., Charbonnier, D., Vos, J. B., Jirasek, A., Peng, S. H., Winkler, A., Allen, A., Wissocq, G., Puigt, G., Dandois, J., Abarca, R. (2016). *Unsteady Aero-Loads from Vortices Shed on A320 Landing Gear Door: CFD compared to flight tests*. AIAA Paper 2016-0803.

[17] Aquilini, C., Abarca, R. (2022). *Modelling of Dynamic Vibration Absorbers to Reduce Landing Gear Doors Vibration of Commercial Transport Aircraft*. IFASD 2022, Madrid, Spain.

[18] Katzenmeier, L., Vidy, C., Kolb, A., Breitsamter, C. (2021). Aeroelastic Wind Tunnel Model for Tail Buffeting Analysis using Rapid Prototyping Technologies. *CEAS Aeronautical Journal*, pp. 633-651.

[19] Katzenmeier, L., Hilfer, M., Stegmüller, J., Breitsamter, C. (2023). Application of fast-response pressure sensitive paint to low-speed vortical flow at high angles of attack. *Experiments in Fluids*, Article 166.

[20] Stegmüller, J., Katzenmeier, L., Breitsamter, C. (2022). Horizontal tail buffeting characteristics at wing vortex flow impact. *CEAS Aeronautical Journal*, pp. 779-796.

NOMENCLATURE

AFLoNext	Active Flow- Loads & Noise control on Next generation wing	HTP	horizontal tail plane
CFD	computational fluid dynamics	LES	large eddy simulation
CSM	computational structural mechanics	PLA	polylactide
DES	detached eddy simulation	RANS	Reynolds averaged Navier Stokes
FEM	finite element model		

COPYRIGHT STATEMENT